J Mater Sci (2007) 42:1638–1648
DOI 10.1007/s10853-006-1096-2

Structure and properties of bulk nanostructured alloys synthesized by flux-melting

T. D. Shen · X. Zhang · K. Han · C. A. Davy · D. Aujla · P. N. Kalu · R. B. Schwarz

Received: 30 May 2006 / Accepted: 2 October 2006 / Published online: 9 January 2007

Abstract Nanomaterials can easily be prepared as thin films and powders, but are much harder to prepare in bulk form. Nanostructured materials are prepared mainly by consolidation, electrodeposition, and deformation. These processing techniques have problems such as porosity, contamination, high cost, and limitations in refining the grain size. Since most bulk engineering metals are initially prepared by casting, we developed a casting technique, flux-melting and melt-solidification, to prepare bulk nanostructured alloys. The casting technique has such advantages as simplicity, low cost, and full density. In our method, Ag–Cu alloys were melted in B_2O_3 flux, which removed most of the impurities, mainly oxides, in the melts. Upon solidifying the melt at a relatively slow cooling rate on the order of 10^1–10^2 K/s a large undercooling of ~0.25 T_m (where T_m is the melting temperature) was achieved. This large undercooling leads to the formation of bulk nanostructured Ag–Cu alloys composed of alternative Ag/Cu lamella and nanocrystals, both ~50 nm in dimension. Our liquid-processed alloys are fully dense and relatively free from contamination. The nanostructured Ag–Cu alloys have similar yield strength in tension and in compression. The as-quenched alloys have yield strength of 400 MPa, ultimate tensile strength (UTS) of 550 MPa, and plastic elongation of ~8%. The UTS was further increased to ~830 MPa after the as-quenched alloy rod was cold drawn to a strain of ~2. The nanostructured Ag–Cu alloys show a high electrical conductivity (~80% that of International Annealed Copper Standard), a slight strain hardening (strain-hardening coefficient of 0.10), and a high thermal stability up to a reduced temperature of 2/3 T_m. Some of these behaviors are different than those found in previous bulk nanostructured materials synthesized by solid state methods, and are explained based on the unique nanostructures achieved by our flux-melting and melt-solidification technique.

T. D. Shen (✉) · R. B. Schwarz
Materials Science and Technology Division, Los Alamos National Laboratory, Mail Stop G755, Los Alamos NM 87545, USA
e-mail: tdshen@lanl.gov

X. Zhang
Department of Mechanical Engineering, Texas A&M University, College Station, TX 77843-3123, USA

K. Han · C. A. Davy · D. Aujla · P. N. Kalu
National High Magnetic Field Laboratory, 1800 E Paul Dirac Dr., Tallahassee, FL 32310, USA

Introduction

Decreasing the grain size of a polycrystalline alloy to the nanometer range is one method one can use to increase the alloy's strength and hardness. Although nanomaterials can easily be prepared as thin films and powders, they are much harder to prepare in *bulk* form. Currently, there are three general methods to prepare *bulk* nanostructured materials, as described below.

Consolidation of nanostructured powders

This synthesis method usually consists of two steps. First, techniques such as mechanical alloying, rapid

solidification, and chemical reaction are used to produce nanocrystalline powders and nanoparticles. The next step, consolidation of the nanostructured powders or particles, is the most difficult step because, to preserve the nanostructure, the consolidation must be done at high pressures and relatively low temperatures [1, 2]. The pressure must be significantly higher than the hardness of the powders and particles, since a lower pressure will not lead to full densification. Any residual porosity would significantly degrade the mechanical and physical properties of the compact [3, 4]. The consolidation temperature must be kelp relatively low to avoid grain growth and recrystallization.

Recently, a one-step in-situ consolidation technique has been developed to synthesize nanocrystalline Cu and Zn with an average grain size of ~20 nm [5, 6]. This technique can provide porosity-free nanocrystalline spheres with a diameter of up to 10 mm and a narrow grain size distribution. The resulting nanocrystalline bulks have probably the best combination of strength and ductility ever achieved in nanocrystalline materials [7]. This technique, however, requires materials with a good extensibility.

In practice, there are few consolidation techniques that work at high pressure and low temperature. One such consolidation technique makes use of high-energy shock waves. Short-duration pressure shocks can be generated by the impact of high-velocity projectiles that are accelerated to the km/s range in a gas-gun, or by explosives. Taking careful measures to trap the momentum of the traveling shock wave, once this wave has traversed the porous specimen, researchers have prepared in the laboratory fully dense inch-diameter nanocrystalline samples [8]. Effective bonding between the particles results from localized melting at the particle boundaries, which flow and fill the cavities between the initial powder compact, and also break up the oxide layers that may cover each particle. The interior of the particles deforms much less and thus remains at near-room-temperature. These cooler regions provide an internal ''quenching'' of the melted interparticle regions. Upon rapidly solidifying the interparticle melt, the whole compact attains the desired nanocrystalline structure. Achieving good interparticle bonding requires a careful control of the shock pressure and shock duration. Too high a pressure leads to excessive melting and homogeneous heating, which destroys the nanostructure of the material, whereas too-short a shock duration does not allow the interparticle melt to solidify before the unavoidable arrival of the release wave [8]. Therefore, there is an optimal window of shock pressure and shock duration within which one can prepare nanocrystalline materials of exceptionally high strength [9]. The main drawbacks of the shock-wave consolidation technique are its high cost and the difficulty in scaling the consolidation technique beyond the inch-diameter coupons that can be prepared in laboratories.

Electrodeposition of nanocrystalline plates

Electrodeposition can be used to prepare nanocrystalline metals and alloys having average grain size of ~5–50 nm [10–13]. Two advantages of this technique are that the products have a narrow distribution of grain sizes and that the microstructure of the product can be controlled to have small-angle grain boundaries [14] or highly twinned grains [15]. The drawbacks of the method are that it can only be used for a rather limited number of chemical systems and that the product is often brittle due to intergranular impurities [16]. Changes in ion concentration during the electrodeposition are known [17, 18] to cause microstructural and compositional inhomogeneities in the product.

Severe plastic deformation of polycrystalline materials

This is perhaps the oldest strengthening method known to man. New variants have been developed in the last decades with the purpose of achieving elevated levels of strain while preserving the product aspect ratio. These new deformation methods include equal-channel angular extrusion (ECAE) [19, 20], high-pressure torsion [20, 21], repetitive corrugation and straightening [22], multiple forging [23], twist extrusion [24, 25], accumulative roll bonding [26–29], and co-deformation of in-situ composites [30–37]. These techniques have been applied to a wide range of crystalline materials with various degrees of success. The main drawback of this technique is its high cost. Another problem has been the lack of a consistent level of tensile strength throughout the bulk product. This problem usually arises from inclusions and/or porosity retained in the heavily deformed product. A third problem is a rather low ductility.

Under certain conditions, bulk polycrystalline materials with nanosize grains can be prepared directly from the melt. For example, a fine lamellar microstructure is often obtained by solidifying a eutectic melt at a relatively fast rate. Solidification theory predicts that the eutectic lamellar spacing is inversely proportional to the undercooling of the melt at the solidification front [38]. This suggests that lamella thicknesses in the nanometer range may be obtained at a sufficiently large degree of undercooling. Factors that favor a large

degree of undercooling are: (a) a fast rate of cooling and (b) the removal of impurities (e.g., oxide particles) that may act as heterogeneous nucleation centers for crystallization. The cooling rate cannot be increased without bounds, however, unless one limits at least one of the dimensions of the solid. This is an intrinsic limitation due to the finite thermal conductivity of the molten alloy. The second factor, the removal of heteronucleants, has been less studied. The degree of undercooling that can be achieved in a rapidly solidified melt at a giving cooling rate is always limited by the onset of homogeneous nucleation, but this limit is seldom, if ever, reached; crystallization is almost always heterogeneous. So, the question arises: can a range of cooling rates and melt purification processes be used to prepare inexpensively centimeter-diameter polycrystalline alloys with crystals in the nanometer range?

In the present work, we applied these simple concepts to the synthesis of a eutectic $Ag_{60}Cu_{40}$ alloy [39]. We used B_2O_3 flux to dissolve or neutralize most of the impurities in the melt that would have competed with the undercooling process. The carefully purified melt was then solidified at a cooling rate of ~10^2 K/s. This cooling rate, being relatively slow, enabled us to prepare 1-cm diameter rods. The microstructure of the as-prepared rods consisted of alternative Ag and Cu lamella, approximately 70 and 30 nm thick, respectively. The as-prepared alloys were fully dense and contained no inclusions. Tensile deformation of the as-prepared rods by drawing enabled us to further reduce the lamellar spacing. In the following we discuss the processing, microstructure, and properties (electrical, elastic, and mechanical) of these alloys.

Experimental

Silver and copper shot (2–6 mm, 99.999% pure) were used as starting materials to prepare the eutectic $Ag_{60}Cu_{40}$ (at%) alloys. The Ag and Cu were placed in a fused-silica tube together with pieces of vitreous B_2O_3 flux. The silica tube was evacuated, filled with pure argon to a pressure slightly higher than 1 atm, and then heated slowly to 1,300 °C to melt the three components. Following melting, the B_2O_3 floated on the surface of the Ag–Cu melt, as schematically shown in Fig. 1. The tube was again evacuated while keeping the melt at 1,300 °C. During this process, bubbles emerged from the melt signifying the loss of water from the flux and oxygen from the Ag–Cu melt. When the bubbling ceased (after approximately 1 h) and the pressure was in the low 10^{-3} Torr range, we filled the

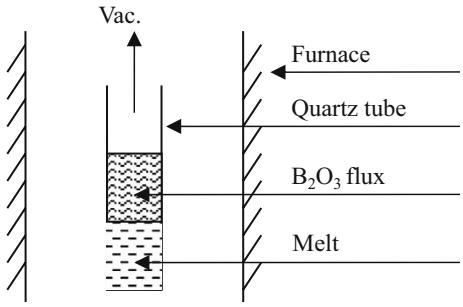

Fig. 1 Schematic description of flux-melting technique

tube with high-purity argon to a pressure slightly higher than 1 atm and then quenched the tube in water. In this way we prepared samples ranging from 3 mm to 10 mm in diameter. Several 4-mm diameter rods are shown in Fig. 2. For some of the experiments, a small fused-silica tube containing a W/Re thermocouple was immersed into the molten Ag–Cu alloy. This thermocouple recorded the melt temperature during the water-quenching process.

Two types of annealing treatments were used to modify the microstructures of the as-cast alloys. The first treatment was an isothermal annealing during which the as-cast alloys were heated in a furnace to a given temperature and isothermally annealed at the temperature for 1 h. The furnace was located inside an argon-filled glove box containing less than 0.1 ppm oxygen. After the annealing the alloys were quenched in aluminum foils. The second treatment was a cold drawing during which the as-cast 10-mm diameter ingots were cold drawn (at room temperature) to 4-mm diameter wires.

The alloys were characterized by X-ray diffraction (XRD), scanning electron microscopy (SEM), transmission electron microscopy (TEM), resistivity, modulus,

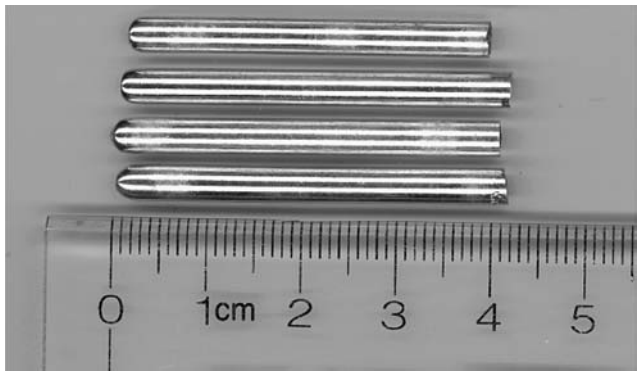

Fig. 2 Optical microscopy image of $Ag_{60}Cu_{40}$ rods with a diameter of 4 mm and a length of approximately 40 mm

hardness, tension, and compression measurements. A rotating anode X-ray diffractometer operated at a voltage of 45 kV and a current of 200 mA, was used for the XRD measurements. The SEM observations were done with a JSM7401F Field Emission Scanning Electron Microscopy (FESEM). The SEM samples were cut from the alloy rod, mechanically polished, and etched in a solution of nitric acid in ethanol for 45–60 s. The TEM observations were carried out with a JEOL 3000F microscope operated at 300 kV. TEM specimens were prepared by mechanically thinning, polishing, and ion milling a 3-mm diameter disk. The resistivity was measured on the alloy rods by a standard four-probe method with a DC current of 1.5–3 A. The Young's, bulk, and shear moduli were measured by Resonant Ultrasound Spectroscopy (RUS) [40]. The microhardness measurements were made on a Micromet-4 tester at loads of 1 kg force on 3-mm diameter disks that were cut from the as-cast rods and then polished using 0.3 μm alumina paste. Tension testing was conducted on samples with a gauge diameter of 1.6 mm and a gauge length of 15 mm. Compression testing was done on cylindrical specimens, 2.9-mm diameter and 5.8-mm long, which were cut from the as-quenched rod by electrical discharge machining. Both tension and compression tests were performed at a strain rate of 2×10^{-4} s^{-1}.

Results

Undercooling

Temperature–time curves measured during water-quenching a 10-mm diameter rod of Ag–Cu alloy (data not shown here) showed a small exothermic peak at approximately 520 °C, which we identified as the recalescence temperature. We estimate the error in the determination of this temperature to be approximately ±30 K. This uncertainty is due to the difficulties in identifying the onset of the recalescence, and to the unavoidable temperature gradient between the melt and the immersed thermocouple. Thus, the undercooling at the onset of crystallization was approximately 260 ± 30 K, which is ~25% of the eutectic temperature (1,053 K). Such a large undercooling in a Ag–Cu melt is possible only if the melt has been carefully purified. The cooling rate close to the recalescence temperature was ~23 K/s. These measurements were performed on a 10-mm diameter ingot. Most likely, even larger cooling rates and undercoolings are achieved during the preparation of smaller diameter rods.

Microstructure

Figure 3 shows an XRD pattern for the as-quenched $Ag_{60}Cu_{40}$ alloy. The alloy consists of *fcc* Ag(Cu) and *fcc* Cu(Ag) solid solutions. We estimated the average crystallite size D using the Scherrer equation [41], $D = 0.9L/\beta\cos\theta$ where L is the wavelength of X-ray, β is the full width at half maximum of the Bragg peak, and θ is the diffraction angle. Using the β of the reflection (111) we obtained an average crystallite size of 45 nm for both the Ag(Cu) and Cu(Ag) phases. This crystallite size agrees with the layer thickness we determined by direct TEM observations, to be discussed below.

The as-quenched alloy contains large grains, with sizes ranging from 100 μm to 500 μm [39]. These grains formed via regular eutectic growth starting from a rather low density of isolated nucleation centers. The shape of the grains reflects the fact that the growth proceeds from the surface of the rods inwards. Figure 4 shows the TEM image of an as-quenched $Ag_{60}Cu_{40}$ alloy rod [39]. The alloy is composed of alternating Ag and Cu lamella, which is the typical microstructure of regularly grown eutectic alloys. The average thickness of the Ag lamellae is $\lambda_{Ag} \sim 70$ nm, and the average thickness of the Cu lamellae is $\lambda_{Cu} \sim 30$ nm. The ratio of the thickness, $\lambda_{Ag}/\lambda_{Cu} = 7/3$, agrees with the eutectic composition. The Ag and Cu lamellae have low densities of grown-in dislocations. The inset is a diffraction pattern from a selected area that covers several adjacent lamellae. This pattern, and others, show that the close-packed {111} planes in Ag and Cu grow parallel to each other.

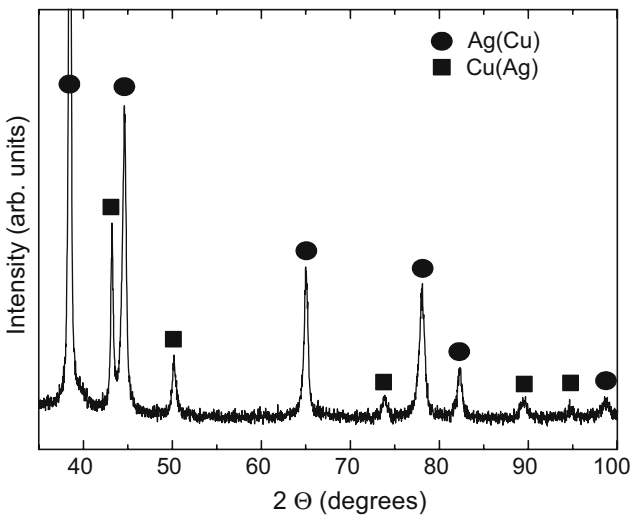

Fig. 3 XRD pattern of as-quenched $Ag_{60}Cu_{40}$ rod

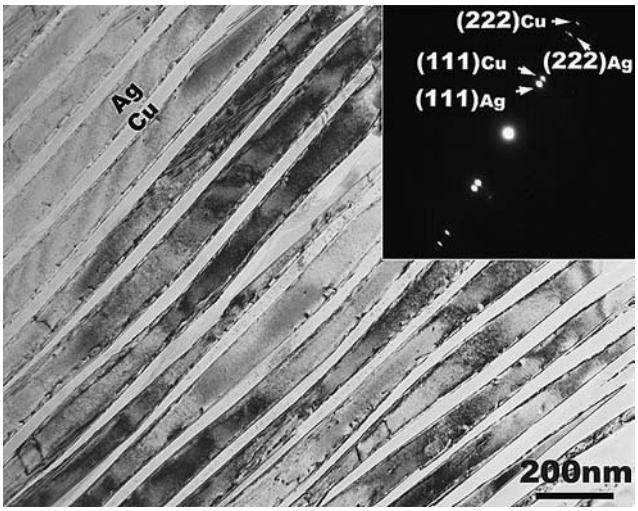

Fig. 4 Bright-field TEM image and the corresponding selected-area diffraction pattern of as-quenched $Ag_{60}Cu_{40}$ rod

Figure 5 shows the SEM images of the cross section of an as-prepared 10-mm diameter rod (Fig. 5(a)) and of the same material after the rod was cold drawn to a diameter of 4 mm (Fig. 5(b)). From these images we determined that the deformation caused the lamellar spacing, ($\lambda_{Ag}+\lambda_{Cu}$), to decrease from ~200 nm to 100 nm. The true strain introduced by this cold-drawing is approximately 2.

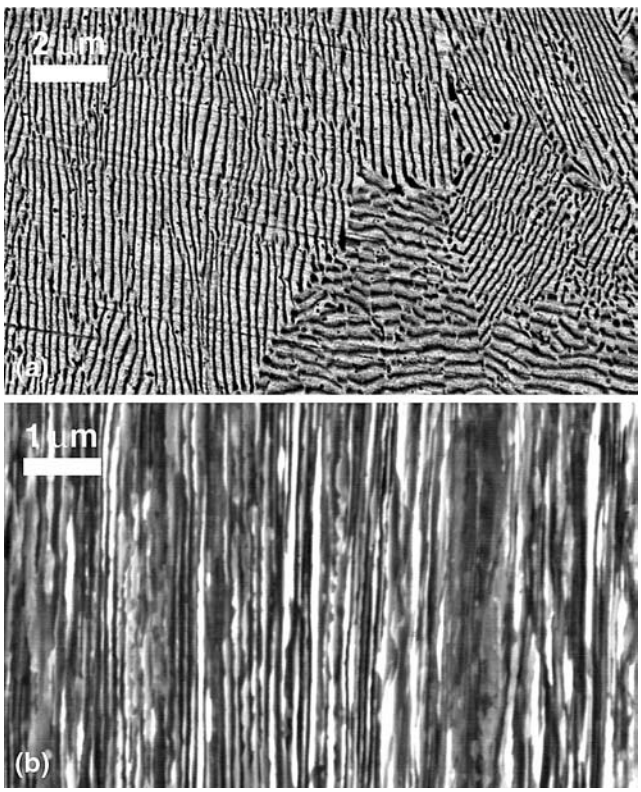

Fig. 5 SEM images of as-quenched and as-drawn $Ag_{60}Cu_{40}$ alloys. (**a**) As-quenched rod with a diameter of 10 mm, (**b**) rod (**a**) after being cold-drawn to a wire with a diameter of 4 mm

Thermal stability

Figure 6(a) shows the lattice parameters of the Ag(Cu) and Cu(Ag) phases following 1-h anneals at the temperatures stated in the abscissa. We determined the lattice parameters using the Bradley and Jay's extrapolation method [42]. Figure 6(b) shows the solute contents deduced from the lattice parameters plotted in Fig. 6(a). The equilibrium solute concentrations of Cu in Ag and Ag in Cu, estimated from the Ag–Cu phase diagram [43], are plotted in Fig. 6(b) as dashed line and dashed-dotted line, respectively. The partial atomic volumes of Cu in Ag, and of Ag in Cu,

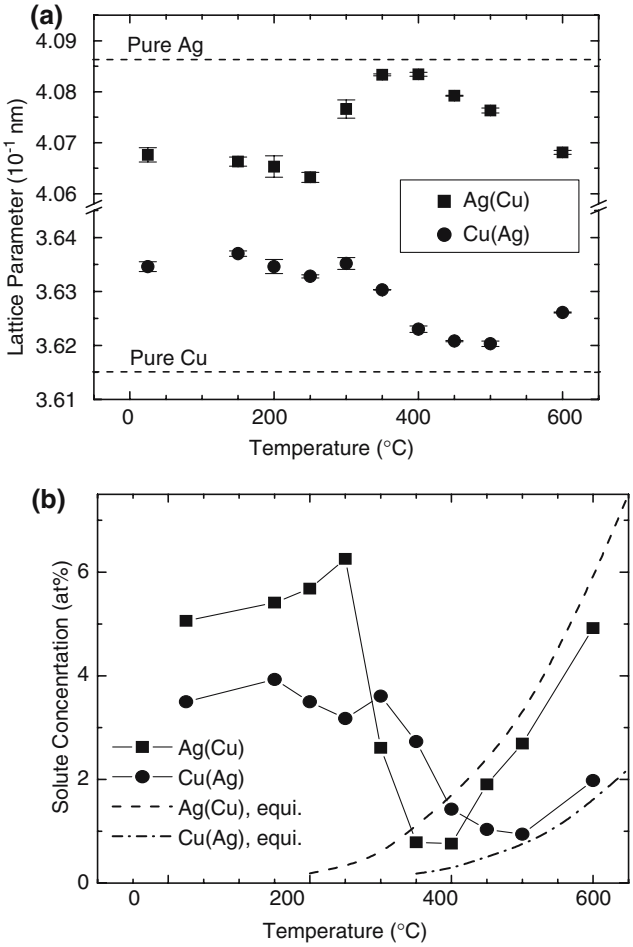

Fig. 6 (**a**) Lattice parameters of *fcc* Ag(Cu) and *fcc* Cu(Ag) in annealed $Ag_{60}Cu_{40}$. Horizontal lines represent the lattice parameters of pure Ag and Cu. (**b**) Solute concentrations of *fcc* Ag(Cu) and *fcc* Cu(Ag) in annealed $Ag_{60}Cu_{40}$. Dashed and dashed-dotted lines represent the equilibrium solute concentrations of Ag(Cu) and Cu(Ag) solid solutions

deviate from a strict Vegard's law. Massalski [44] compiled data for the change in the lattice parameters of various solid solutions, and quoted the values $(1/a)(da/dc) = -0.09$ for Ag(Cu) solution, and $(1/a)(da/dc) = 0.155$ for Cu(Ag) solution. Using these values we derived the solute concentrations in the Cu and Ag phases of our alloys, both in the as-quenched initial condition and after annealing for 1 h at various temperatures. Figure 6(b) indicates that the solute concentrations of the Ag and Cu phases in the as-quenched alloy are significantly larger than the equilibrium solute concentrations, which are negligible at room temperature. Therefore, the Ag(Cu) and Cu(Ag) solutions are supersaturated.

For annealing temperatures below 300 °C, the Cu and Ag have some degrees of lattice distortion relaxation and solutes cannot leave the Ag and Cu matrices, respectively, because the diffusivity is too low. Above 300 °C more relaxation occurs and the compositions of the two phases approach their equilibrium values at those temperatures. Thus the lattice parameters of the Ag phase increase whereas those of the Cu phase decrease. However, above approximately 400 °C, the solute content in the Ag and Cu phases increases reflecting the increase in the equilibrium solubility with increasing temperature.

Figure 7 shows the crystallite sizes (D), estimated from the Scherrer formula, of the Ag(Cu) and Cu(Ag) solid solution phases as a function of annealing temperature. The initial crystallite size is 45 nm, which is approximately equal to half of the lamellae thickness, $(\lambda_{Ag}+\lambda_{Cu})/2$. This size remains constant up to an annealing temperature of 400 °C, which is 64% of the melting temperature of eutectic $Ag_{60}Cu_{40}$ alloys. Therefore, our nanostructured $Ag_{60}Cu_{40}$ alloys have a relatively high thermal stability. Figure 7 further suggests that the mechanical properties of the lamellar Ag–Cu alloy should remain constant for annealing temperatures below approximately 400 °C, as discussed below.

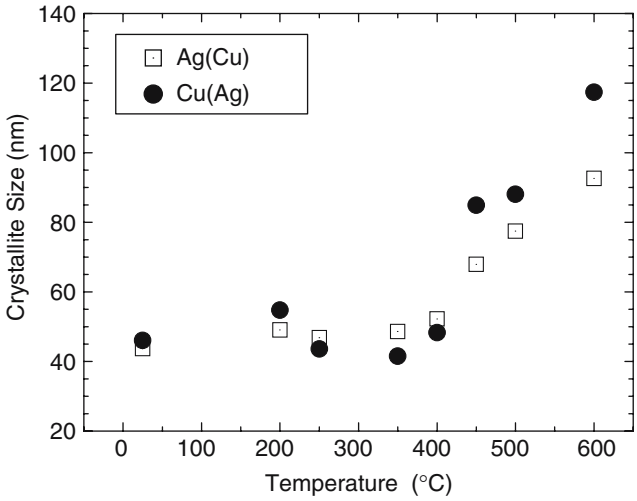

Fig. 7 Temperature dependence of the crystallite size in *fcc* Ag and *fcc* Cu determined from the width of the (111) Bragg peak measured by X-ray diffraction

Electrical conductivity

Table 1 gives the conductivity of the $Ag_{60}Cu_{40}$ alloy in the as-cast and cold drawn conditions. The as-cast alloy has conductivity of 79% IACS (International Annealed Copper Standard). Cold drawing reduces the conductivity by approximately 5%. For both as-cast and cold-drawn rods, the conductivity at 77 K is approximately three times of that at room temperature. Note that the cold drawing increases the strength by 50% (to be discussed below). Thus, further drawing can be used to increase the strength of the alloy while retaining a high conductivity, which is critical to developing high-strength/high-conductivity alloys for practical applications.

Elastic moduli

Table 2 lists the Young's (E), bulk (B), and shear (G) of Ag, Cu, polycrystalline and nanocrystalline $Ag_{60}Cu_{40}$ alloys. The moduli of polycrystalline $Ag_{60}Cu_{40}$ are calculated using the rule-of-mixtures. Compared to their polycrystalline counterparts, the nanocrystalline $Ag_{60}Cu_{40}$ alloys have similar B but lower E and G.

Mechanical properties

Figure 8 shows the microhardness of as-cast $Ag_{60}Cu_{40}$ as a function of distance, which is measured from the center to the surface on the cross section. The average hardness is 1.45 ± 0.11 GPa. However, the center has a

Table 1 Electrical conductivity of as-cast and cold-drawn $Ag_{60}Cu_{40}$ alloys measured at 77 and 300 K

	As-cast	Cold-drawn
σ (RT, MS/m)	46.1 ± 0.6 (79% IACS[a])	43.5 ± 0.8 (75% IACS[a])
σ (77 K, MS/m)	149 ± 7	119 ± 3
σ (77 K)/σ (RT)	3.2	2.7

Both the as-cast and clod-drawn rods have a diameter of 4 mm. The diameter of the rod before cold drawing is 10 mm

[a] IACS (International Annealed Copper Standard) = 58 MS/m, which is the volume conductivity of pure copper at 20 °C

Table 2 Young's (E), shear (G), and bulk (B) moduli of polycrystalline (Ag, Cu and $Ag_{60}Cu_{40}$) and nanocrystalline ($Ag_{60}Cu_{40}$) materials

	Ag (polycry.)	Cu (polycry.)	$Ag_{60}Cu_{40}$ (polycry.)	$Ag_{60}Cu_{40}$ (nanocry.)
E (GPa)	83	130	97.8	88.4
B (GPa)	103	138	114.0	114.3
G (GPa)	30	48	35.7	32.2

The moduli of Ag and Cu were taken from the literature whereas those of polycrystalline $Ag_{60}Cu_{40}$ were calculated using the rule-of-mixtures. The moduli of nanocrystalline ($Ag_{60}Cu_{40}$) were experimentally measured

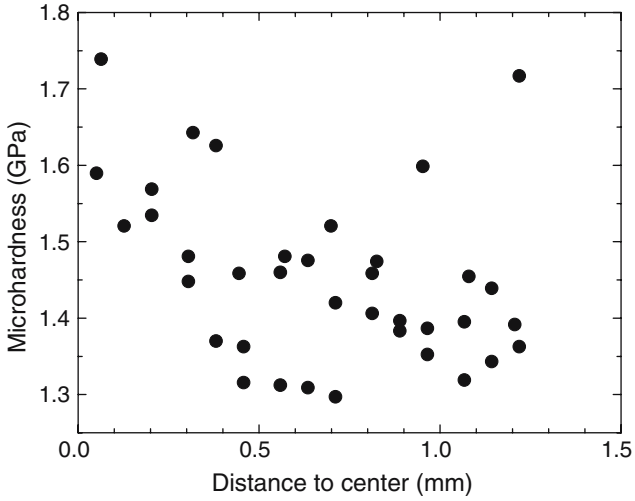

Fig. 8 Microhardness as a function of distance away from the rod center in as-quenched $Ag_{60}Cu_{40}$ rod

hardness of ~1.6–1.7 GPa, which is ~20% higher than the hardness (~1.3–1.4 GPa) in the surface.

Figure 9 shows stress–strain curves for the $Ag_{60}Cu_{40}$ alloys measured in tension and compression [39]. The alloys have (1) yield strength ($\sigma_{0.2}$) of about 400 MPa—approximately one order of magnitude larger than that [45, 46] of polycrystalline Ag or Cu; (2) a tensile strain-to-fracture of ~8%; and (3) a strain-hardening exponent $n = d(\ln\sigma)/d(\ln\varepsilon) = 0.10 \pm 0.02$ during both tension and compression, where σ and ε represent true stress and true plastic strain. Because of the quite large strain hardening, the ultimate tensile strength (UTS) reaches 550 MPa, ~40% higher than the yield strength (400 MPa). Note that the yield strength in tension (400 MPa) is slightly higher than that (370 MPa) in compression. This is because the gauge part (~1.6 mm in diameter) of the alloy being tested in tension corresponds to the central region of the as-cast rod (~3 mm in diameter) whereas the compression test is performed on the whole cross-sectional area (~3 mm in diameter) of the rod. That the

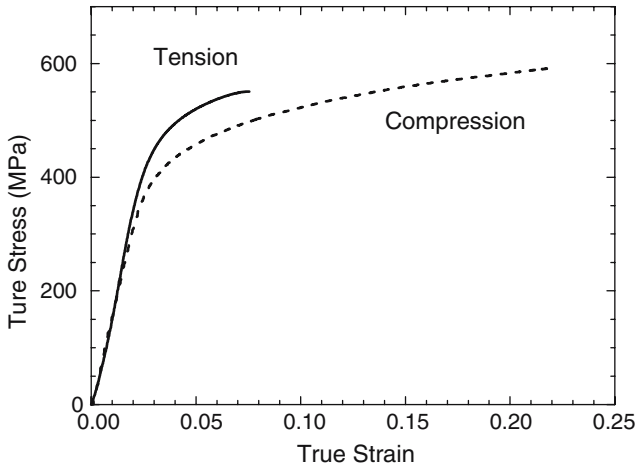

Fig. 9 Stress–strain curves for as-quenched $Ag_{60}Cu_{40}$ rods measured in tension and compression

yield strength is slightly higher near the center of the as-quenched rod agrees with the hardness data shown in Fig. 8.

Shown in Fig. 10 are the tensile stress–strain curves for the $Ag_{60}Cu_{40}$ alloys after various thermo-mechanical treatments. Notice that the 300 °C annealing reduces the stresses and increases both the total elongation (strain-to-fracture) and homogeneous elongation slightly. The 600 °C annealing further increases the ductility but at the expense of a drastic decrease in strength. Cold drawing alone has the reverse effect, increasing the strength at the expense of a decrease in ductility. The yield strength and UTS of cold-drawn nanostructured $Ag_{60}Cu_{40}$ are ~810 and 830 MPa, respectively, significantly higher than those, 400 and

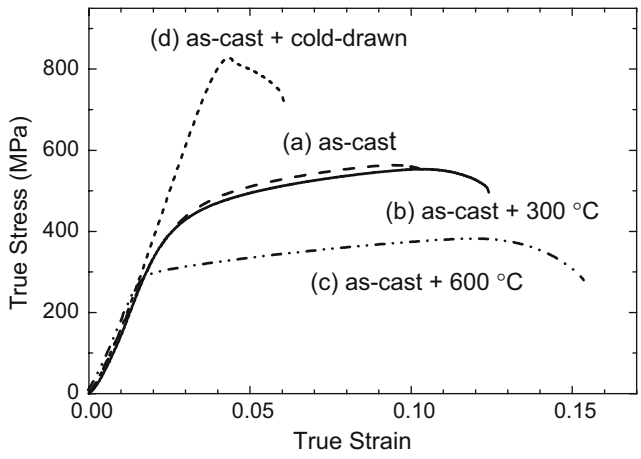

Fig. 10 Tensile stress–strain curves for $Ag_{60}Cu_{40}$ rods after various thermal and mechanical treatments. (a) As-cast, (b) as-cast rod after annealing at 300 °C for 1 h, (c) as-cast rod after annealing at 600 °C for 1 h, and (d) as-cast dia-10 mm rod cold drawn to dia-4 mm rod

550 MPa, of as-cast nanostructured $Ag_{60}Cu_{40}$. However, the plastic elongation decreases from ~8% to 3% after cold drawing. The optimization of the fabrication conditions may lead to an increase in flow stress while retaining a few percent ductility.

Figure 11 summarizes the yield strength, UTS, and elongation-to-fracture for samples that were annealed and then tested at room temperature. In agreement with Fig. 7, the mechanical properties do not deteriorate unless the annealing temperature exceeds 400 °C.

Figure 12 compares the ultimate tensile strength (UTS) of the present $Ag_{60}Cu_{40}$ (at%) alloys to those of previously studied $Cu_{83.6}Ag_{16.4}$ (at%) [47] and $Cu_{85.9}Nb_{14.1}$ (at%) [48] alloys prepared by severe plastic deformation. The abscissa in this figure is the plastic strain used to increase the strength of the alloy. The figure shows that at a given plastic strain our lamellar eutectic nanostructured alloys provide the highest UTS. This is because in our alloy we are already starting from an ultra-fine (~50 nm) lamellar microstructure.

Discussion

The microstructures that form during melt solidification can adopt various morphologies, such as eutectic and dendritic, and these can be present in a wide range of size scales. Alloy casting is often done at near-eutectic composition because the melt has better casting behavior (low solidification temperature and low viscosity) and the solidified composite has good mechanical properties (relatively small grains/crystallites and thus high strength). In Cu-based $Cu_{84}Ag_{16}$

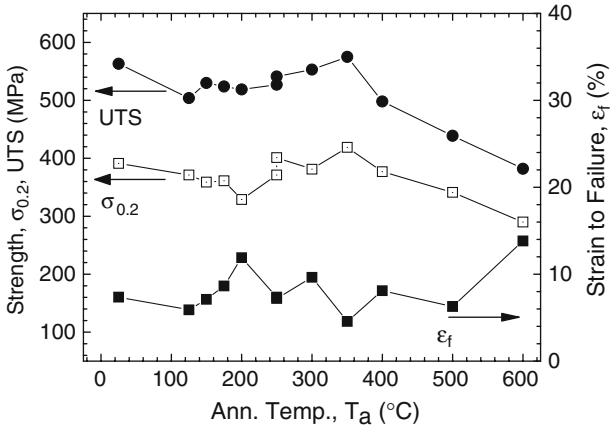

Fig. 11 Ultimate tensile strength (UTS), yield strength for a plastic strain of 0.2% ($\sigma_{0.2}$), and strain to failure (σ_f) of eutectic Ag–Cu alloy as a function of annealing temperature for annealing times of 1 h

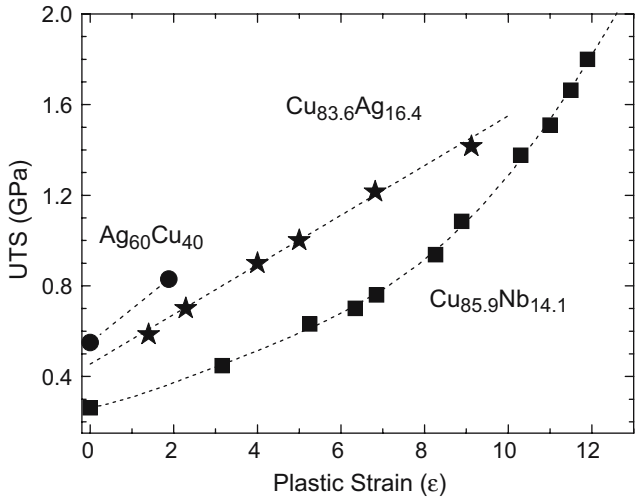

Fig. 12 Comparison of the mechanical properties as a function of plastic strain for the alloys developed in the present work to those of previous works

alloys, increasing the cooling rate to ~3×10^4 K/s leads to a Ag/Cu lamellar spacing of ~100 nm in a solidified wire with a diameter of ~30 μm [49, 50]. However, *bulk* metallic materials cast at a slower rate (<10^2 K/s) do not have nanocrystalline structures. This is because the slow cooling rate, which usually leads to a small undercooling and a relatively high solidification temperature, cannot effectively suppress the growth of crystals. The present study suggests that this problem can be solved by using a flux-melting technique. During the flux melting, the B_2O_3 flux removes most oxide particles from the melt. This significantly lowers the density of heterogeneous nucleation centers, resulting in a large undercooling at a relatively slow cooling rate. Clearly, it is this large undercooling that leads to the formation of nanolayered Ag(Cu) and Cu(Ag). For regular eutectic growth in undercooled melts, lamellar eutectics prefer to grow under ''extreme conditions''—crystal growth occurs at the minimum undercooling ΔT for a given crystal growth velocity V. In this way the eutectic lamellar spacing (λ) is inversely proportional to the undercooling [38]. Despite the fact that the large undercooling helps refine the lamellar structure, the present alloy melt may not solidify exactly under the extreme conditions. Figure 8 indicates that the central region is harder than the surface region of the solidified rod. This suggests that, when compared with the surface, the central region has a finer microstructure. However, the cooling rate and the resultant undercooling in the central region could be the lowest over the whole cross section of the solidified rod.

The present nanostructured Ag–Cu alloys show that the yield strength in tension is slightly higher than that

in compression. In contrast, a strong tension–compression asymmetry has been observed in bulk nanocrystalline Cu prepared by compacting Cu nanoparticles [51], with the tensile strength being approximately 30–50% of the compressive strength. Furthermore, the ductility measured during tension was less than 1% [2]. Since this nanocrystalline Cu had several percent porosity, it is reasonable to assume that the observed tension–compression asymmetry and low ductility are not intrinsic behavior of nanomaterials but the effects of the processing artifacts (residual porosity).

Strengthening in our nanocrystalline alloys arises from the crystal size refinement and from solid-solution hardening. The hardening from crystal size refinement can be estimated from the Hall–Petch relation, $\sigma = \sigma_o + K\, d^{-1/2}$, where σ is the yield stress and d is the crystallite size. With $\sigma_{o,Cu} = 0.06$ GPa, $K_{Cu} = 2.05$ GPa/nm$^{1/2}$ [52], $\sigma_{o,Ag} \approx 0.11$ GPa, and $K_{Ag} \approx 1.40$ GPa/nm$^{1/2}$ [53], the Hall–Petch relation averaged over the Ag and Cu volume fractions in the present $Ag_{60}Cu_{40}$ alloy composition predicts a yield strength of 337 MPa. Therefore, crystal refinement seems to provide the majority of the strength. We found no measurements for the solid-solution hardening in metastable Ag(Cu) and Cu(Ag) alloys. An estimate of the solid solution hardening can be obtained from the known strength values for Cu(Ge) alloys [54], which have a value of $d(\ln a)/d(c)$ similar to that in our Ag–Cu alloys, where a is the lattice parameter and c the solute content [55]. This comparison predicts a solid-solution strengthening in Ag–Cu alloys (with a solute content of about 5 at%) of 10 MPa. Dislocation activities are effectively confined in small crystals. It is thus the small crystallite size rather than the large grain size that determines the strength of materials. Similar phenomena have been observed in nanostructure metallic multilayer thin films [56]. At a layer thickness of 10 nm or less, the average columnar grain size within each constituent layer is typically greater than the layer thickness. In these scenarios, the hardness of multilayer films is dominated by layer thickness (which is usually similar to the crystal size), rather than the columnar grain sizes.

The lattice distortion introduces internal stresses in both Cu and Ag components [57]. Both Cu and Ag have the *fcc* crystallographic structure but Cu has a smaller lattice constant than Ag. Therefore, misfit dislocations form at the interfaces between Cu and Ag in bulk samples. When the spacing between Cu/Cu or Ag/Ag reduces to the magnitude of smaller than 100 nm, both the Cu and Ag phases intend to reduce the numbers of misfit dislocations in the unit volume [58]. To accommodate the misfit and the reduced numbers of dislocations, Ag reduces its lattice parameter and therefore is in compression whereas Cu increases its lattice parameter and in tension. These stresses are perpendicular to the normal of the interfaces [57, 58]. In the direction parallel to the interfaces, the internal stresses in different components have an opposite signs. When the materials are subject to an external load, the total stresses applied to an individual component are the sum of the external and internal stresses. Cu has relatively large modulus but with internal tensile stresses. Further tensile loading introduces plastic deformation. Therefore the apparent modulus of the Cu component is smaller than that of Cu without any initial external stresses. Similar arguments are applicable to Ag. Therefore, the measured Young's modulus is different from the value calculated by a rule of mixture. The bulk modulus represents the modulus under hydrostatic pressure. As the composites have a tetragonal lattice distortion as addressed in references [57, 58], the influences of the internal stresses on modulus in different orientations tend to be cancelled out. Hence, the bulk modulus is similar to what calculated by a rule of mixture. The other reason that is responsible for the slightly reduced Young's and shear moduli observed in the nanocrystalline $Ag_{60}Cu_{40}$, when compared with their polycrystalline counterparts, may be due to the high density of interphase interfaces and grain boundaries [3].

Our nanocrystalline Ag–Cu alloy has a strain-hardening exponent of about 0.10, significantly smaller than that of polycrystalline Cu, typically 0.30–0.35 [59]. Compared with their polycrystalline counterparts, nanocrystalline metals and alloys usually have a lower strain-hardening exponent. This is because dislocation pile-up, which frequently occurs in large-grained polycrystalline materials, is less likely in nanocrystalline materials due to the high density of the interfaces that provide sinks for dislocations. In addition, in nanostructured materials most of the dislocations generated by plastic deformation may take the form of dislocation dipoles, which only generate short-range stress fields and thus contribute little to the overall strength of materials [60]. However, the non-zero strain-hardening exponent in our as-cast Ag–Cu alloy suggests that strain still causes the increase in dislocation density and thus contributes to the enhanced strength of strained alloy, as shown in Fig. 9. This suggests that the cast nanomaterials have more potential to reach high (UTS) strength than the deformed nanomaterials, as discussed below.

Whether nanostructured materials will be hardened by straining depends on not only crystal size but also the structure of grain boundary and grain interior. In many nanostructured materials with a crystal size of

~200–300 nm prepared by severe plastic deformation (SPD), straining usually either causes elastoplasticity (constant stress on straining) [61] or softening (decreased stress on straining) [29, 62]. This may be understood by the fact that the high density of dislocations generated during the SPD significantly increases the recovery rate of dislocations generated during further straining. As such, the dislocation annihilation rate may reach or exceed the dislocation generation rate, leading to elastoplasticity or softening. In comparison, our as-cast Ag–Cu alloy with a crystal size of ~50 nm has a much lower density of pre-existing dislocations inside the lamella. When the materials are subject to plastic deformations, the generation rate of dislocations exceeds the annihilation rate of dislocations. This results in strain hardening.

Our supersaturated nanostructured Ag–Cu alloy has a high thermal stability. Crystal growth occurs for temperatures above 400 °C, which is ~2/3 of the melting temperature. One reason for the high thermal stability may be ascribed to the solute drag effect, which suppresses the diffusion of matrix atoms. This is supported by the fact that the starting temperature for crystal growth (Fig. 7) is similar to the temperature where most solute atoms are rejected from their solution matrix (Fig. 6). Both spheriodization and coarsening, which accompany crystal growth, may occur at temperatures above 400 °C. This indicates that the majority of the Cu–Ag interfaces are relatively stable. In this system, spheriodization occurs before coarsening [63]. However, the first step of the spheriodization is to increase the interface energies by rotating the interface boundaries from the semicoherent to incoherent boundaries. Such activities require relatively high thermal activity energy thus high temperatures.

Drawing our as-cast Ag–Cu rod significantly increase the strength. This can be understood by two effects: lamellar refinement and strain hardening. The drawing refines lamellar spacing, as shown in Fig. 5. This should strengthen the drawn alloy based on the Hall–Petch relationship. The strain hardening is confirmed in Fig. 9 and can be attributed to the increased dislocation density upon straining. The well-known strain hardening theory suggests that the strength scales with the square root of the dislocation density.

Conclusions

We have used a flux-melting and melt-solidification technique to prepare impurity- and porosity-free nanostructured eutectic $Ag_{60}Cu_{40}$ alloys. The flux removes oxide heteronuclents from melt, allowing us to achieve a large undercooling upon solidification. This results in the formation of nanostructured Ag–Cu alloys composed of alternative Ag/Cu lamella with an average single-layer thickness of ~50 nm.

The yield strength of nanostructured $Ag_{60}Cu_{40}$ in tension is similar to that in compression because the as-quenched nanostructured alloys are fully dense. The as-quenched alloys have high yield strength (~400 MPa), high UTS (550 MPa), and good ductility (~8% plastic elongation). After being drawn to a strain of ~2, the yield and ultimate strength of Ag–Cu alloy increase to 810 and 830 MPa, respectively. In principal, the present processing technique should be applicable to other eutectic or near-eutectic alloys, such as Fe–C.

The nanostructured Ag–Cu alloys show softened Young's and shear moduli when compared with their polycrystalline counterparts. This may be attributed to the lattice distortion and the high density of interfaces. The as-cast alloy has a high electrical conductivity, 79% that of IACS. The conductivity decreases by only ~5% IACS after cold drawing to a strain of ~2. The combination of high strength and high conductivity is desired for many applications.

The nanostructured Ag–Cu alloy has strain hardening, which is mainly because the as-cast alloy is relatively free from dislocations. Further deformation should accumulate dislocations because there is no significant recovery induced by the pre-existing dislocations.

The achieved high thermal stability can be ascribed to the stable semicoherent interfaces. Relatively large thermal activity energy is required to render any coarsening of the composites.

Acknowledgements This work was supported by the Laboratory Directed Research & Development (LDRD) program of the Los Alamos National Laboratory and the National High Magnetic Field Laboratory (NHMFL) at the Los Alamos National Laboratory. Part of the work was performed at the National High Magnetic Field Laboratory, which was supported by NSF Cooperative Agreement No. DMR-0084173, by the State of Florida, and by the DOE. Part of the work was supported by a PREM program by NSF.

References

1. Gleiter H (1989) Prog Mater Sci 33:223
2. Sanders PG, Eastman JA, Weertman JR (1997) Acta Mater 45:4019
3. Shen TD, Koch CC, Tsui TY, Pharr GM (1995) J Mater Res 10:2892
4. Koch CC, Morris DG, Lu K, Inoue A (1999) MRS Bull 24:54
5. Youssef KM, Scattergood RO, Murty KL, Koch CC (2004) Appl Phys Lett 85:929
6. Zhang X, Wang H, Koch CC (2004) Rev Adv Mater Sci 6:53
7. Youssef KM, Scattergood RO, Murty KL, Horton JA, Koch CC (2005) Appl Phys Lett 87:091904

8. Schwarz RB, Kasiraj P, Vreeland T, Ahrens TJ (1984) Acta Metall 32:1243
9. Kasiraj P, Vreeland T, Schwarz RB, Ahrens TJ (1984) Acta Metall 32:1235
10. Wang N, Wang Z, Aust KT, Erb U (1997) Mater Sci Eng A 237:150
11. Ebrahimi F, Zhai Q, Kong D (1998) Scripta Mater 39:315
12. Karimpoor AA, Erb U, Aust KT, Palumbo G (2003) Scripta Mater 49:651
13. Saber KH, Koch CC, Fedkiw PS (2003) Mater Sci Eng A 341:174
14. Lu L, Sui ML, Lu K (2000) Science 287:1463
15. Lu L, Shen YF, Chen XH, Qian LH, Lu K (2004) Science 304:422
16. Wang YM, Cheng S, Wei QM, Ma E, Nieh TG, Hamza A (2004) Scripta Mater 51:1023
17. Czerwinski F, Sepunar JA (1999) Nanostruct Mater 11:669
18. Wolf H, Guan Z, Li X, Wichert Th (2001) Hyperfine Interact 136/137:281
19. Valiev RZ, Krasilnikov NA, Tsenev NK (1991) Mater Sci Eng A 137:35
20. Valiev RZ, Korznikov AV, Mulyukov RR (1993) Mater Sci Eng A 168:141
21. Valiev RZ, Islamgaliev RK, Alexandrov IV (2000) Prog Mater Sci 45:103
22. Zhu YT, Jiang Honggang, Huang Jianyu, Lowe TC (2001) Metall Mater Trans 32A:1559
23. Salishchev GA, Valiakhmetov OR, Valitov VA, Muktarov SK (1994) Mater Sci Forum 170–172:121
24. Beygelzimer Y, Orlov D, Varyukhin V (2002) In: Zhu YT, Langdon TG, Mishra RS, Semiatin SL, Saran MJ, Lowe TC (eds) Ultrafine grained materials. 2002 TMS Annual Meeting and Exhibition, Seattle, p 297
25. Stolyarov VV, Beygelimev YE, Orlov DV, Valiev RZ (2005) Phys Met Metall 99:204
26. Atzmon M, Verhoeven JD, Gibson ED, Johnson WL (1984) Appl Phys Lett 45:1052
27. Shen TD, Quan MX, Wang JT (1994) J Mater Sci 28:394
28. Saito Y, Utsunomiya H, Tsuji N, Sakai T (1999) Acta Mater 47:579
29. Huang X, Hansen N, Tsuji N (2006) Science 312:249
30. Wood JT, Embury JD, Ashby MF (1997) Acta Mater 45:1099
31. Embury JD, Han K (1998) Curr Opin Solid State Mater Sci 3:304
32. Leprince-Wang Y, Han K, Huang Y, Yu-Zhang K (2003) Mater Sci Eng A 351:214
33. Han K, Vasquez AA, Xin Y, Kalu PN (2003) Acta Mater 51:767
34. Embury JD, Fisher RM (1966) Acta Metall 14:147
35. Han K, Mottishaw TD, Smith GDW, Edmonds DV, Stacey AG (1995) Mater Sci Eng A 190:207
36. Han K, Mottishaw TD, Smith GDW, Edmonds DV (1994) Mater Sci Technol 10:955
37. Han K, Smith GDW, Edmonds DV (1995) Metall Mater Trans A 26A:1617
38. Biloni H, Boettinger WJ (1996) In: Cahn RW, Haasen P (eds) Physical metallurgy. Elsevier Science B V, Amsterdam, ch 8
39. Shen TD, Schwarz RB, Zhang X (2005) Appl Phys Lett 87:141906
40. Schwarz RB, Vuorinen JF (2000) J Alloys Compd 310:243
41. Guinier A (1963) X-ray diffraction. Freeman, San Francisco, p 124
42. Klug HP, Alexander LE (1974) X-ray diffraction procedure. John Wiley & Sons, New York, p 591
43. Murray JL (1984) Metall Trans 15A:261
44. Massalski TB (1996) In: Cahn RW, Haasen P (eds) Physical metallurgy. Elsevier Science B.V., Amsterdam, ch 3
45. Carreker RP (1957) Trans AIME 209:112
46. Carreker RP, Hibbard WR (1953) Acta Metall 1:654
47. Han K, Embury JD, Sims JR, Campbell LJ, Schneider-Muntau HJ, Pantsyrnyi VI, Shikov A, Nikulin A, Vorobieva A (1999) Mater Sci Eng A 267:99
48. Spitzig WA, Pelton AR, Laabs FC (1987) Acta Metall 35:2427
49. Han K, Embury JD, Petrovic JJ, Weatherly GC (1998) Acta Mater 46:4691
50. Han K, Hirth JP, Embury JD (2001) Acta Mater 49:1537
51. Sanders PG, Youngdahl CJ, Weertman JR (1997) Mater Sci Eng A 234:77
52. Iyer RS, Frey CA, Sastry SML, Waller BE, Buhro WE (1999) Mater Sci Eng A 264:210
53. Qin XY, Wu XJ, Zhang LD (1995) Nanostruct Mater 5:101
54. Haasen P (1996) In: Cahn RW, Haasen P (eds) Physical metallurgy. Elsevier Science B V, Amsterdam, p 2009
55. Massalski TB (1996) In: Cahn RW, Haasen P (eds) Physical metallurgy. Elsevier Science B V, Amsterdam, p 182
56. Misra A, Verdier M, Kung H, Embury JD, Hirth JP (1999) Scripta Mater 41:973
57. Han K, Lawson AC, Wood JT, Embury JD, Von Dreele RB, Richardson JW Jr (2004) Phil Mag 84:2579
58. Han K, Embury JD, Lawson AC, Von Dreele RB, Richardson JW Jr, Wood JT (2004) In: Schneider-Muntau H (ed) VIIIth International conference on megagauss magnetic field generation and related topics. World Scientific, Singapore, p 154
59. Hertzberg RW (1983) Deformation and fracture mechanics of engineering materials. John Wiley & Sons, New York, p 17
60. Ma E, Shen TD, Wu XL (2006) Nat Mater 5:515
61. Champion Y, Langlois C, Guerin-mailly S, Langlois P, Bonnentien JL, Hytch MJ (2003) Science 300:310
62. Valiev RZ, Alexandrov IV, Zhu YT, Lowe TC (2002) J Mater Res 17:5
63. Gleiter H (1996) In: Cahn RW, Haasen P (eds) Physical metallurgy. Elsevier Science B V, Amsterdam, p 878